This article has been accepted for publication in a future issue of this journal, but has not been fully edited. Content may change prior to final publication. Citation information: DOI 10.1109/TIE.2015.2407851, IEEE Transactions on Industrial Electronics

Reactive Power Control of Three-Phase Grid-Connected PV System During Grid Faults Using Takagi-Sugeno-Kang Probabilistic Fuzzy Neural Network Control

Faa-Jeng Lin, *Senior Member*, *IEEE*, Kuang-Chin Lu, *Member*, *IEEE*, Ting-Han Ke, Bo-Hui Yang, and Yung-Ruei Chang, *Member, IEEE*

***Abstract*—An intelligent controller based on Takagi-Sugeno-Kang type probabilistic fuzzy neural network with asymmetric membership function (TSKPFNN-AMF) is developed in this study for the reactive and active power control of a three-phase grid-connected photovoltaic (PV) system during grid faults. The inverter of the three-phase grid-connected PV system should provide a proper ratio of reactive power to meet the low voltage ride through (LVRT) regulations and control the output current without exceeding the maximum current limit simultaneously during grid faults. Therefore, the proposed intelligent controller regulates the value of reactive power to a new reference value which complies with the regulations of LVRT under grid faults. Moreover, a dual mode operation control method of the converter and inverter of the three-phase grid-connected PV system is designed to eliminate the fluctuation of DC-link bus voltage under grid faults. Furthermore, the network structure, online learning algorithm, and convergence analysis of the TSKPFNN-AMF are described in detail. Finally, some experimental results are illustrated to show the effectiveness of the proposed control for the three-phase grid-connected PV system.**

***Index Terms*—Asymmetric membership function (AMF), grid faults, low voltage ride through (LVRT), photovoltaic system, reactive power control, Takagi-Sugeno-Kang type probabilistic fuzzy neural network (TSKPFNN).**

I. Introduction

Fuzzy neural network (FNN) inherits the learning ability of neural networks and the inference technology of fuzzy systems, which can be used as an effective method for dealing with complex nonlinear systems. Therefore, many researchers have used the FNN approaches to represent complex plants and construct advanced controllers [1], [2]. Moreover, since the Takagi-Sugeno-Kang type fuzzy neural network (TSKFNN) provides more powerful representation than the Mamdani type FNN does, the TSKFNN is one of the most adopted FNN schemes [3], [4]. Since the dimensions of the standard Gaussian or triangular membership function (MF) are directly extended in asymmetric membership function (AMF), not only the learning capability of the networks can be upgraded but also the number of fuzzy rules can be optimized. Thus, the AMF has been adopted in several approaches to optimize the number of fuzzy rules and improves the control precisions [5]. Furthermore, a probabilistic fuzzy neural network (PFNN) is a neural network implementation of Parzen nonparametric probability density function estimation and Bayes classification rule, the PFNN can handle the uncertainties in the control system effectively [6], [7]. Based on the merits of TSKFNN, AMF and PFNN, the Takagi-Sugeno-Kang type probabilistic fuzzy neural network with asymmetric membership function (TSKPFNN-AMF) is proposed in this study. Since the proposed TSKPFNN-AMF is the combination of the characteristics of TSKFNN with AMF and PFNN, it is a new intelligent control scheme and good at dealing with uncertainty, complexity, and strong nonlinearity. The proposed TSKPFNN-AMF can be adopted to develop a system with fast learning capability for nonlinear systems with uncertainties and can be applied in some areas such as modeling, classifying, and control problems.

Owing to the environmental issues and the deregulation of the electric power distribution industry, the fast growth of renewable energy sources and distributed generation sources (DGSs) has increased the connection of inverters to the public grid largely. Among the renewable energy sources, the photovoltaic (PV) technology is one of the candidates to pick up a sizeable chunk of power shortfall in the future. However, the control of PV systems is a challenge because of the uncertainty in the availability of the input power [8]. Moreover, the increased amount of grid-connected DGSs over the power system can create instability or even lead to outages when electrical disturbances appear in the system. One of the most challenging disturbances is the plunge of the grid voltage, known as voltage sags [9], [10]. In order to maintain a stable power system and minimize the negative effects of large number of DGSs integration on the reliability of power grids, different countries have defined various low voltage ride through (LVRT) regulations for DGSs. E.ON has defined the limit curve for the voltage pattern at the

Manuscript received May 6, 2014; revised September 8, 2014 and November 25, 2014; accepted February 3, 2015.

This work was supported by the National Science Council, Taiwan, R. O. C. through its grant NSC 101-2221-E-008-104-MY3.

F. J. Lin is with the Department of Electrical Engineering, National Central University, Chungli 320, Taiwan (corresponding author to provide phone:886-3-4227151 ext. 34532; fax: 886-3-4255830; e-mail: linfj@ee.ncu.edu.tw).

K. C. Lu is with the Department of Electrical Engineering, National Central University, Chungli 320, Taiwan, and also with the Internet of Things Laboratory, Telecommunication Laboratories, Chunghwa Telecom Co., Ltd. Taoyuan 32661, Taiwan (e-mail: gcl@cht.com.tw).

T. H. Ke and B. H. Yang are with the Department of Electrical Engineering, National Central University, Chungli 320, Taiwan (e-mail: t903871802@gmail.com; bohuei8197@gmail.com).

Y. R. Chang is with the Institute of Nuclear Energy Research, Atomic Energy Council, Taoyuan 32546, Taiwan (e-mail: raymond@iner.gov.tw).

This article has been accepted for publication in a future issue of this journal, but has not been fully edited. Content may change prior to final publication. Citation information: DOI 10.1109/TIE.2015.2407851, IEEE Transactions on Industrial Electronics

point of common coupling (PCC) for type 2 generating plants [11]. Grid regulations also demand reactive current injection during fault conditions to support grid stability [11], in which 1pu of reactive current is required as the sag depth reaches 50%. The E.ON LVRT regulation will be used in this study to determine the ratio of the required reactive current during grid faults.

Since the power quality of a three-phase inverter deteriorates drastically in the presence of grid faults with unbalanced voltages, some grid fault control schemes have been proposed [12]-[18] under unbalanced grid voltage. A selective active power quality control based on several different current reference generating methods was proposed in [12]. Moreover, three different control schemes based on symmetrical components and linear quadratic regulator have been proposed to fulfill LVRT requirements under voltage dips [13]. Furthermore, a design method was developed to search for the control parameter values that minimize the peak currents during grid voltage sags [14]. In [15, 16], a flexible reactive current injection scheme was proposed which provides voltage support during voltage sag by injecting reactive current via both positive and negative sequences. A method which is similar to [15] was proposed for the compensation of reactive power and voltage support by considering the network with resistive impedance [17]. In addition, a reactive current injection method without exceeding the current limit of the inverter and to compensate the transformer flux offset within the grid-connected invert was proposed in [18]. However, the balance of the active power between the power generated by the DGSs and the power delivered into the grid under grid faults are not considered in the above references.

The proposed TSKPFNN-AMF controller is adopted in this study to control the injection of active and reactive power of the PV system during grid faults. The DC-link bus voltage and PV maximum power point tracking (MPPT) control are also considered for the sake of ensuring the power balance during grid faults. Moreover, mathematical analysis of the injected currents during the grid faults is carried out in order to develop the proposed controller. Furthermore, the network structure, online learning algorithm of network parameters and proof of convergence of the proposed TSKPFNN-AMF controller are discussed in detail. In addition, several cases of grid faults are tested and discussed in order to evaluate the performance of the proposed controller. In this study, Section II presents the three-phase grid-connected PV system and analyzes the output voltages and currents of the inverter during grid faults. In Section III, the dual mode operation control method of the boost converter and the three-phase inverter of the three-phase grid-connected PV system during grid faults are discussed. Section IV presents the TSKPFNN-AMF controller in detail. In Section V, the features of the proposed controller are examined by some experimental results. Finally, Section VI presents the conclusions of this study.

II. Three-Phase Grid-Connected PV System under Grid Faults

The schematic diagram of the three-phase grid-connected PV system considered in this study is shown in Fig. 1. The

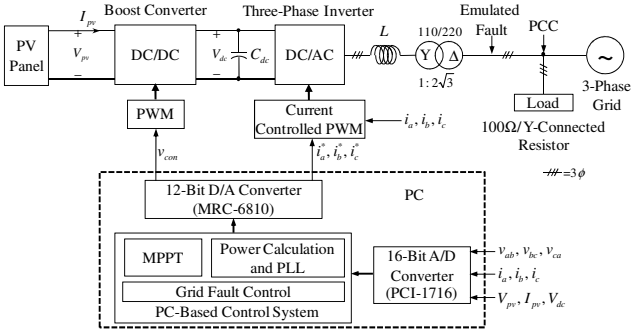

Fig. 1. Three-phase grid-connected PV system.

TABLE I
Parameters in Experimental Set-Up

DC-link voltage	V_{dc}	200V
DC-link capacitor	C_{dc}	3360μF
Grid connection inductor	L	10mH
Inverter output voltage	v_{ab}, v_{bc}, v_{ca}	110Vrms line to line, 60Hz
Inverter maximum current	I_{max}	5Arms (7.1A peak current)
Emulated PV panel		V_{oc}: 185.6V, I_{sc}: 6.599A, 1kW
Switching frequency	f_{sw_C}, f_{sw_I}	18kHz, 10kHz

PV panel is emulated by a Chroma 62100H-600S PV simulator operating at 153 VDC output voltage with maximum output power 1kW. Utility grid is emulated by three programmable 2kVA single-phase KIKUSUI PCR2000LE AC power supplies feeding a Y-connected 100Ω/phase resistive load, and connected to the 2kVA three-phase inverter with a 3kVA Y-△ transformer. The 2kVA three-phase inverter with output 110Vrms line to line voltages is connected to the boost converter through a 3360μF DC-link capacitor C_{dc} and connected to the Y-Δ transformer with three 10mH/phase coupling inductors. The switching frequencies of the boost converter f_{sw_C} and three-phase inverter f_{sw_I} are set at 18kHz and 10kHz respectively. Some parameters of the experimental set-up are listed in Table I. The PC includes a PC-based control system, a 16-bit A/D converter (PCI-1716), and a 12-bit D/A converter (MRC-6810) interfaces. In the PC-based control system, the SIMULINK control package is adopted for the implementation of the proposed algorithms including the MPPT control, power calculation and phase-locked loop (PLL) block, and grid fault control. The sampling rate of the A/D converter is set to 2kHz. The boost converter and the three-phase inverter are interconnected by a DC-link capacitor, and the control of DC-link bus voltage V_{dc} balances the power flow in the system. The boost converter boosts the PV panel DC output voltage V_{pv} up to V_{dc} and accomplishes MPPT in normal operation. The adopted MPPT method is the voltage-based perturb-and-observe scheme [19]. Moreover, in normal condition of the grid, the three-phase inverter injects all the generated active power into the grid. On the other hand, in fault conditions of the grid, the reactive power control of the three-phase inverter can mitigate the influences of voltage sag by injecting additional reactive current to ride through the disturbance and support the grid voltage [15]. Furthermore, the injected current has to meet the LVRT

This article has been accepted for publication in a future issue of this journal, but has not been fully edited. Content may change prior to final publication. Citation information: DOI 10.1109/TIE.2015.2407851, IEEE Transactions on Industrial Electronics

regulations and without going beyond the inverter current limit simultaneously.

A. Voltages and Currents during Grid Faults

The line voltages of the three-phase inverter can be converted into the phase voltages as follows:

$$\begin{bmatrix} v_a \\ v_b \\ v_c \end{bmatrix} = \frac{1}{3}\begin{bmatrix} 1 & 0 & -1 \\ -1 & 1 & 0 \\ 0 & -1 & 1 \end{bmatrix}\begin{bmatrix} v_{ab} \\ v_{bc} \\ v_{ca} \end{bmatrix} \tag{1}$$

where $[v_{ab}, v_{bc}, v_{ca}]^T$ indicates the line voltages and $[v_a, v_b, v_c]^T$ represents the phase voltages. In this study, the calculations of the active and reactive power are based on phase voltages and phase currents. Moreover, the Clarke transformation is applied to express measured voltages in the stationary reference frame [20] as v_α, v_β.

$$v_{\alpha\beta} = \begin{bmatrix} v_\alpha \\ v_\beta \end{bmatrix} = \sqrt{\frac{2}{3}}\begin{bmatrix} 1 & -\frac{1}{2} & -\frac{1}{2} \\ 0 & \frac{\sqrt{3}}{2} & -\frac{\sqrt{3}}{2} \end{bmatrix}\begin{bmatrix} v_a \\ v_b \\ v_c \end{bmatrix} \tag{2}$$

The $v_{\alpha\beta}$ voltage vector rotating on the $\alpha\beta$ plane can also be expressed on a synchronous reference frame by using the Park transformation. The voltage vector $[v_d, v_q]^T$ is expressed as

$$\begin{bmatrix} v_d \\ v_q \end{bmatrix} = \begin{bmatrix} \cos(\theta_e) & \sin(\theta_e) \\ -\sin(\theta_e) & \cos(\theta_e) \end{bmatrix}\begin{bmatrix} v_\alpha \\ v_\beta \end{bmatrix} \tag{3}$$

where the subscript p, q indicates the synchronous reference frame axes. The synchronous reference frame PLL algorithm reported in [21] is used in this study to obtain the angular position θ_e of the dq synchronous reference frame. Furthermore, the three-phase inverter currents i_a, i_b, i_c can also be transferred into the synchronous reference frame i_d, i_q as

$$\begin{bmatrix} i_d \\ i_q \end{bmatrix} = \sqrt{\frac{2}{3}}\begin{bmatrix} \cos(\theta_e) & \cos(\theta_e - \frac{2}{3}\pi) & \cos(\theta_e + \frac{2}{3}\pi) \\ -\sin(\theta_e) & -\sin(\theta_e - \frac{2}{3}\pi) & -\sin(\theta_e + \frac{2}{3}\pi) \end{bmatrix}\begin{bmatrix} i_a \\ i_b \\ i_c \end{bmatrix} \tag{4}$$

The current q component i_q is controlled to manage the active power and typically to perform the DC-link bus voltage regulation while the current d component i_d is controlled to manage the reactive power. Thus, the output active and reactive power of the three-phase inverter is [21]

$$P = \frac{3}{2}(v_d i_d + v_q i_q) \text{ and } Q = \frac{3}{2}(v_q i_d - v_d i_q) \tag{5}$$

P and Q represent the instantaneous output active and reactive power respectively. Assuming that the grid current vector is in phase with the grid voltage resulted in $v_d = 0$, the active and reactive power will therefore be proportional to i_q and i_d respectively as follows:

$$P = \frac{3}{2}v_q i_q \text{ and } Q = \frac{3}{2}v_q i_d \tag{6}$$

B. Reactive and Active Power Control

The percentage of the required compensation reactive current I_r^* is a function of the voltage sag V_{sag} which can be expressed as [11]

$$I_r^* = \begin{cases} 0\% & , V_{sag} \le 0.1 \\ 200V_{sag}\% & , 0.1 < V_{sag} \le 0.5 \\ 100\% & , V_{sag} > 0.5 \end{cases} \tag{7}$$

$$V_{sag} = \left(1 - \frac{\min\left(|v_a|_{rms}, |v_b|_{rms}, |v_c|_{rms}\right)}{V_{base}}\right) \text{pu} \tag{8}$$

where V_{base} is the base value of voltage which equals 63.5Vrms in this study; $|v_a|_{rms}$, $|v_b|_{rms}$, $|v_c|_{rms}$ are the rms values of the voltages v_a, v_b, v_c respectively. The output current of the three-phase inverter should not exceed the upper current limit is one of the important features of the proposed method. The apparent power of the inverter will be changed due to the voltage sag at PCC under grid faults. If V_{sag} is greater than 0.1pu, then a voltage sag occurs on the grid side and the reactive power injection is initiated. In order to meet the LVRT requirement and avoid exceeding the maximum current limit of the three-phase inverter, the maximum apparent power of the three-phase inverter $|S|$ is obtained as follows:

$$|S| = \left(|v_a|_{rms} + |v_b|_{rms} + |v_c|_{rms}\right) I_{\max} \tag{9}$$

where $I_{\max}$ is the rms value of the maximum current limit. Then, the reference value of the injected reactive power Q^* and active power reference value P^* are expressed as

$$Q^* = |S| I_r^* \text{ and } P^* = |S|\sqrt{1 - I_r^{*2}} \tag{10}$$

Therefore, the instantaneous output reactive and active power of the three-phase inverter Q and P are controlled to follow Q^* and P^* by the proportional-integral (PI) or TSKPFNN-AMF controllers during grid faults.

III. Control Method during Grid Faults

In order to inject the active power and reactive power to the grid and avoid exceeding the three-phase inverter maximum current limit during grid faults, P^* may be adjusted to be less than the extracted power of PV panel P_{pv}. This phenomenon could raise the DC-link bus voltage to excess upper limit due to the power imbalance and cause the PV system to disconnect from the grid. A dual mode control method is proposed in this study for the active and reactive power controls during grid faults. If P^* is greater than P, then P_{pv} can be totally delivered into the grid without exceeding $I_{\max}$ via the three-phase inverter by controlling V_{dc}. Therefore, the boost converter can be operated at the normal condition, i.e. the MPPT mode (mode I). On the other hand, when P is greater than P^*, the boost converter stops the tracking of the maximum power point and starts to track P^*. Moreover, the power balance between the boost converter and the three-phase inverter can be held by controlling V_{dc}. This case is named as mode II in this study. Figure 2 shows the algorithm of the dual mode control method. The dual mode control method is used to determine which mode should be operated in the boost converter and the three-phase inverter for keeping the power balance between the boost converter

This article has been accepted for publication in a future issue of this journal, but has not been fully edited. Content may change prior to final publication. Citation information: DOI 10.1109/TIE.2015.2407851, IEEE Transactions on Industrial Electronics

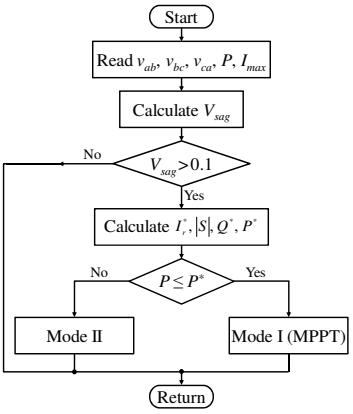

Fig. 2. Algorithm of dual mode operation control method.

and the three-phase inverter.

IV. TSKPFNN-AMF CONTROLLER

The three-phase grid-connected PV system, which includes PV panel, boost converter, three-phase inverter and grid, can be regarded as a nonlinear system with uncertainties. There are some other problems of the three-phase grid-connected PV system, such as the change of temperature and irradiance alters system operating point. Thus, it is very difficult to develop a physical nonlinear model for the system. Hence, for a three-phase grid-connected PV system using traditional PI control, the parameters of PI controller are usually tuned by trial and error to achieve the best control performance considering the stability requirement for a specific operating point. Although the PI controller has been widely used in industries for various control applications, the main disadvantage of the PI controller is that the desired control performance cannot be guaranteed in the presence of plant parameter variations and unknown external disturbances. Since the design of the proposed TSKPFNN-AMF controller does not require mathematical models, the aforementioned problems can be solved. In addition, the proposed TSKPFNN-AMF controller possesses the abilities of online learning, approximating nonlinear systems and confronting uncertainties.

The six-layer structure of TSKPFNN-AMF controller is shown in Fig. 3(a), which consists of the input layer (layer 1), membership layer (layer 2), probabilistic layer (layer 3), TSK type fuzzy inference mechanism layer (layer 4), rule layer (layer 5), and output layer (layer 6), with two inputs and one output. Moreover, the *j*th fuzzy if-then rule of the proposed TSKPFNN-AMF controller is realized as follows:

$$R^j: \text{If } x_1 \text{ is } M_1^j \text{ and } x_2 \text{ is } M_2^j, \text{ then } T_k \text{ is } \sum_i c_{ik} x_i \qquad (11)$$

where R^j is the *j*th rule; x_i is the input of the TSKPFNN-AMF controller and $i = 1, 2$; M_1^j and M_2^j are the fuzzy sets; T_k is the output of TSK type fuzzy inference mechanism; c_{ik} is the adjustable weights. Furthermore, the signal propagation and the basic function in each layer of the TSKPFNN-AMF controller are introduced as follows:

Layer 1 (input layer):

The nodes of this layer pass the input variables x_1, x_2 to the next layer. For every node in this layer, the node input and the node output are described as:

$$net_i^1(N) = x_i^1,\ y_i^1(N) = f_i^1(net_i^1(N)) = net_i^1(N),\ i = 1, 2 \qquad (12)$$

where $x_1^1 = e$, $\dot{x}_1^1 = \dot{e} = x_2^1$; N denotes the *N*th iterations and y_i^1 is the layer 1 node output. In this study, the input variables are $e = V_{dc}^* - V_{dc}$ for the mode I active power control, $e = P^* - P$ for the mode II active power control and $e = Q^* - Q$ for the reactive power control during grid faults.

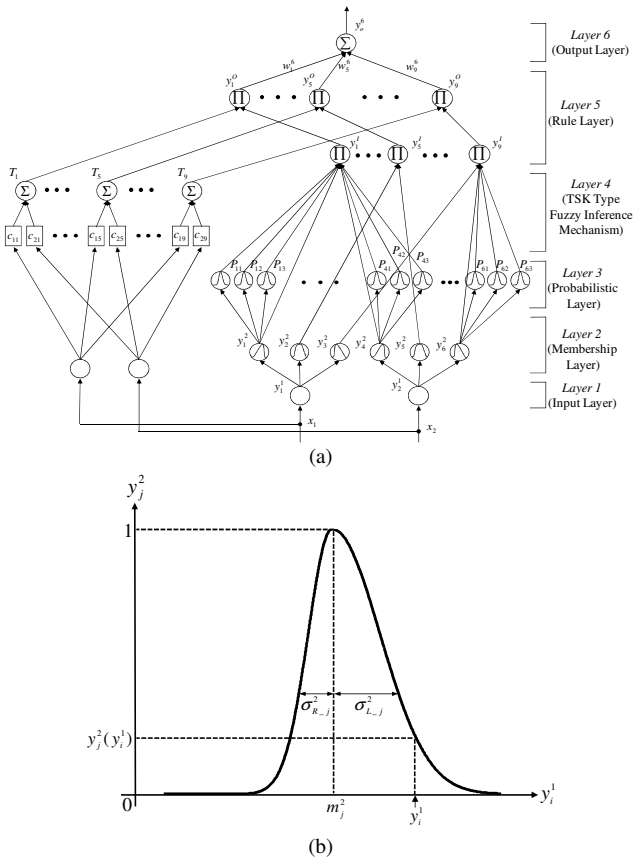

Fig. 3. (a) Structure of TSKPFNN-AMF controller. (b) Asymmetric Gaussian function in membership layer of TSKPFNN-AMF controller.

Layer 2 (membership layer):

In this layer, each node utilizes an asymmetric Gaussian function to realize the fuzzification operation in the TSKPFNN-AMF controller as shown in Fig. 3(b). The node input and output of this layer are presented as:

$$net_j^2(N) = \begin{cases} -\dfrac{(y_i^1(N) - m_j^2(N))^2}{(\sigma_{L\_j}^2(N))^2}, & -\infty < y_i^1(N) \le m_j^2 \\ -\dfrac{(y_i^1(N) - m_j^2(N))^2}{(\sigma_{R\_j}^2(N))^2}, & m_j^2 < y_i^1(N) < \infty \end{cases} \qquad (13)$$

$$y_j^2(N) = f_j^2(net_j^2(N)) = \exp\left(net_j^2(N)\right) \qquad (14)$$

where m_j^2 is the mean of the asymmetric Gaussian function in the *j*th term associated with the *i*th input variable; $\sigma_{L\_j}^2$ and $\sigma_{R\_j}^2$ are, respectively, the left-sided and right-sided standard deviation of the asymmetric Gaussian function in the *j*th term associated with *i*th input variable; y_j^2 is the layer 2 node output.

Layer 3 (Probability Layer):

The general form for these nodes of this layer can be expressed as:

This article has been accepted for publication in a future issue of this journal, but has not been fully edited. Content may change prior to final publication. Citation information: DOI 10.1109/TIE.2015.2407851, IEEE Transactions on Industrial Electronics

$$P_{jp}(N) = f_{jp}(y_j^2(N)) = \exp\left[-\frac{(y_j^2(N)-m_{jp}^3)^2}{(\sigma_{jp}^3)^2}\right] \quad (15)$$
$$, j = 1, 2, \cdots, 6; p = 1, 2, 3$$

where $P_{jp}(N)$ is the output of the *p*th node of the *j*th input variable; m_{jp}^3 and σ_{jp}^3 are the mean and standard deviation of the Gaussian function respectively. Moreover, the probabilistic layer of the TSKPFNN-AMF controller can be used to handle the effect of random noise and stochastic uncertainties existing in the process [22]. Furthermore, reference [23] has shown that the exact form of the probability function is not critical to the effectiveness of the network. Therefore, the parameters of the probability function can be set to be constants for the sake of reducing the computation load. The weights m_{jp}^3 and σ_{jp}^3 are all set to constants, where m_{jp}^3 is set to be -1 for $p = 1$, to be 0 for $p = 2$, and to be 1 for $p = 3$, and σ_{jp}^3 is set to be 1.

Layer 4 (TSK Type Fuzzy Inference Mechanism Layer):

In this layer, the output of the TSK type fuzzy inference mechanism is a linear combination of the input variables. The *k*th node output is expressed as:

$$T_k(N) = \sum_i c_{ik}(N) x_i(N), i = 1,2; k = 1, 2, \cdots, 9 \quad (16)$$

Layer 5 (Rule Layer):

The first part of this layer consists of the output of layer 2 $y_j^2(N)$ and layer 3 $P_{jp}(N)$ to multiply, which is denoted by Π, to get the product. The *k*th node output of the first part of this layer is expressed as:

$$y_k^I(N) = y_r^2(N) y_l^2(N) S_r(N) S_l(N), r = 1, 2, 3 \; ; l = 4, 5, 6; k = 3(r-1) + (l-3) \quad (17)$$

$$S_j(N) = \prod_p P_{jp}(N), \; j = 1, 2, \cdots, 6; \; p = 1, 2, 3 \quad (18)$$

where $S_j(N)$ is the production of the node output of layer 3 $P_{jp}(N)$, which corresponds to the *j*th node of layer 2. The second part is the output of this layer, which is the production of the output of the first part $y_k^I(N)$ and the output of layer 4 $T_k(N)$. The output of each node *k* is

$$y_k^O(N) = T_k(N) y_k^I(N), k = 1, 2, \cdots, 9 \quad (19)$$

where $y_k^O(N)$ is the *k*th node output of the rule layer.

Layer 6 (Output Layer):

The single node *o* in this layer is labeled with ∑, which computes the overall output as the summation of all input signals.

$$net_o^6(N) = \sum_k w_k^6(N) y_k^O(N), o = 1; k = 1, 2, \cdots, 9 \quad (20)$$

$$y_o^6(N) = f_o^6(net_o^6(N)) = net_o^6(N), o = 1 \quad (21)$$

where the connecting weight $w_k^6(N)$ is the output action strength of the *o*th output associated with the *k*th rule; $y_k^O(N)$ represents the *k*th input to the node of layer 6. Moreover, $y_o^6(N) = i_q^*$ is for the active power control and $y_o^6(N) = i_d^*$ is for the reactive power control in the three-phase inverter.

A. Online Learning Algorithm of TSKPFNN-AMF Controller

The central part of the back propagation (BP) learning algorithm for the TSKPFNN-AMF controller concerns how to recursively obtain a gradient vector in which each element in the learning algorithm is defined as the derivative of an energy function with respect to a parameter of the network. To describe the online learning algorithm of the TSKPFNN-AMF controller for the input command tracking using a supervised gradient decent method, first the energy function $E(N)$ is defined as:

$$E(N) = \frac{1}{2}(y^*(N) - y(N))^2 = \frac{1}{2}e^2(N) \quad (22)$$

where *e(N)* represents the tracking error in the learning process of the TSKPFNN-AMF controller for each discrete time *N*; $y^*(N)$ and $y(N)$ represent the desired output and the current output of the system. Then the learning algorithm is described as follows:

Layer 6:

The error term to be propagated is given by:

$$\delta_o^6 = -\frac{\partial E}{\partial y_o^6(N)} = -\frac{\partial E}{\partial y}\frac{\partial y}{\partial y_o^6(N)} \quad (23)$$

The weight is updated by the amount:

$$\Delta w_k^6 = -\eta_1 \frac{\partial E}{\partial w_k^6(N)} = -\eta_1 \frac{\partial E}{\partial y_o^6(N)}\frac{\partial y_o^6(N)}{\partial w_k^6(N)} = \eta_1 \delta_o^6 y_k^O \quad (24)$$

where the factor η_1 is the learning rate. The connective weight w_k^6 is updated according to the following equation:

$$w_k^6(N+1) = w_k^6(N) + \Delta w_k^6 \quad (25)$$

Layer 5:

In this layer, there are two error terms need to be calculated and propagated:

$$\delta_k^O = -\frac{\partial E}{\partial y_k^O(N)} = -\frac{\partial E}{\partial y_o^6(N)}\frac{\partial y_o^6(N)}{\partial y_k^O(N)} = \delta_o^6 w_k^6 \quad (26)$$

$$\delta_k^I = -\frac{\partial E}{\partial y_k^I(N)} = -\frac{\partial E}{\partial y_k^O(N)}\frac{\partial y_k^O(N)}{\partial y_k^I(N)} = \delta_k^O T_k \quad (27)$$

Layer 4:

In this layer, the error term to be propagated is given by:

$$\delta_k^4 = -\frac{\partial E}{\partial T_k(N)} = -\frac{\partial E}{\partial y_k^O(N)}\frac{\partial y_k^O(N)}{\partial T_k(N)} = \delta_k^O y_k^I \quad (28)$$

The weight c_{ik} is updated by the amount:

$$\Delta c_{ik} = -\eta_2 \frac{\partial E}{\partial c_{ik}(N)} = -\eta_2 \frac{\partial E}{\partial T_k(N)}\frac{\partial T_k(N)}{\partial c_{ik}(N)} = \eta_2 \delta_k^4 x_i \quad (29)$$

where the factor η_2 is the learning rate. The connective weight Δc_{ik} is updated according to the following equation:

$$c_{ik}(N+1) = c_{ik}(N) + \Delta c_{ik} \quad (30)$$

Layer 2:

The error term to be propagated is given by:

$$\delta_j^2 = -\frac{\partial E}{\partial net_j^2(N)} = -\frac{\partial E}{\partial y_k^I(N)}\frac{\partial y_k^I(N)}{\partial y_j^2(N)}\frac{\partial y_j^2(N)}{\partial net_j^2(N)} = \begin{cases} h_j \sum_r \delta_k^I y_k^I, \; j = 1, 2, 3; r = 1, 2, 3; k = 3(j-1) + r \\ h_j \sum_r \delta_k^I y_k^I, \; j = 4, 5, 6; r = 1, 2, 3; k = j + 3(r-2) \end{cases} \quad (31)$$

$$h_j = 1 - y_j^2 \sum_p \frac{y_j^2 - m_{jp}^3}{(\sigma_{jp}^3)^2}, \; p = 1, 2, 3 \quad (32)$$

Applying the chain rule, the update laws of the mean of the

This article has been accepted for publication in a future issue of this journal, but has not been fully edited. Content may change prior to final publication. Citation information: DOI 10.1109/TIE.2015.2407851, IEEE Transactions on Industrial Electronics

asymmetric Gaussian function m_j^2 is:

$$\Delta m_j^2 = -\eta_3 \frac{\partial E}{\partial m_j^2} = -\eta_3 \frac{\partial E}{\partial net_j^2(N)} \frac{\partial net_j^2(N)}{\partial m_j^2(N)} = \begin{cases} \eta_3 \delta_j^2 \dfrac{2(y_i^1 - m_j^2)}{(\sigma_{L\_j}^2)^2}, & -\infty < y_i^1 \le m_j^2,\ j = 1, 2, \cdots, 6 \\ \eta_3 \delta_j^2 \dfrac{2(y_i^1 - m_j^2)}{(\sigma_{R\_j}^2)^2}, & m_j^2 < y_i^1 < \infty,\ j = 1, 2, \cdots, 6 \end{cases} \quad (33)$$

The update rules of $\sigma_{L\_j}^2$ and $\sigma_{R\_j}^2$ are:

$$\Delta\sigma_{L\_j}^2 = -\eta_4 \frac{\partial E}{\partial \sigma_{L\_j}^2} = -\eta_4 \frac{\partial E}{\partial net_j^2(N)} \frac{\partial net_j^2(N)}{\partial \sigma_{L\_j}^2(N)} = \eta_4 \delta_j^2 \frac{2(y_i^1 - m_j^2)^2}{(\sigma_{L\_j}^2)^3},\ j = 1, 2, \cdots, 6 \quad (34)$$

$$\Delta\sigma_{R\_j}^2 = -\eta_5 \frac{\partial E}{\partial \sigma_{R\_j}^2} = -\eta_5 \frac{\partial E}{\partial net_j^2(N)} \frac{\partial net_j^2(N)}{\partial \sigma_{R\_j}^2(N)} = \eta_5 \delta_j^2 \frac{2(y_i^1 - m_j^2)^2}{(\sigma_{R\_j}^2)^3},\ j = 1, 2, \cdots, 6 \quad (35)$$

where the factors η_3, η_4 and η_5 are the learning rates. The mean, left-sided, and right-sided standard deviation of the asymmetric Gaussian function are updated according to the following equations:

$$m_j^2(N+1) = m_j^2(N) + \Delta m_j^2 \quad (36)$$

$$\sigma_{L\_j}^2(N+1) = \sigma_{L\_j}^2(N) + \Delta\sigma_{L\_j}^2 \quad (37)$$

$$\sigma_{R\_j}^2(N+1) = \sigma_{R\_j}^2(N) + \Delta\sigma_{R\_j}^2 \quad (38)$$

Since the exact calculation of the Jacobian of the system, $\partial y / \partial y_o^6(N)$ shown in (23) is difficult to be determined due to the uncertainties of the three-phase grid-connected PV system. To overcome this problem, a delta adaptation law is adopted as follows [5]:

$$\delta_o^6 \cong (y^* - y) + (\dot{y}^* - \dot{y}) = e + \dot{e} \quad (39)$$

where $\dot{y}^*$ and $\dot{y}$ are the first derivatives of y^* and y respectively. Moreover, the parameters w_k^6, c_{ik}, m_j^2, $\sigma_{L\_j}^2$, and $\sigma_{R\_j}^2$ are updated by using (25), (30), (36), (37), and (38) respectively. Furthermore, in the initial stage of the TSKPFNN-AMF controller, the values of w_k^6, c_{ik}, $\sigma_{L\_j}^2$, and $\sigma_{R\_j}^2$ are initialized with 0, 1, 1, and 1 respectively; the values of m_1^2, m_2^2, m_3^2, m_4^2, m_5^2, and m_6^2 are initialized with -1, 0, 1, -1, 0, and 1 respectively; the learning rates are initially untrained with zero.

B. Convergence Analyses of the TSKPFNN-AMF Controller

The selection of the values of the learning rate parameters of the TSKPFNN-AMF controller has a significant effect on the network performance. Therefore, in order to train the TSKPFNN-AMF controller online effectively, the varied learning rates, which guarantee the convergence of the tracking errors based on the analysis of a discrete-type Lyapunov function, have been derived as follows [7]:

$$\eta_1 = \frac{E(N)/5}{R_1 + \varepsilon}, \text{ where } R_1 = \sum_{k=1}^{9} \left(\frac{\partial E}{\partial y_o^6(N)} \frac{\partial y_o^6(N)}{\partial w_k^6} \right)^2 \quad (40)$$

$$\eta_2 = \frac{E(N)/5}{R_2 + \varepsilon}, \text{ where } R_2 = \sum_{k=1}^{9} \sum_{i=1}^{2} \left(\frac{\partial E}{\partial T_k(N)} \frac{\partial T_k(N)}{\partial c_{ik}} \right)^2 \quad (41)$$

$$\eta_3 = \frac{E(N)/5}{R_3 + \varepsilon}, \text{ where } R_3 = \sum_{j=1}^{6} \left(\frac{\partial E}{\partial net_j^2(N)} \frac{\partial net_j^2(N)}{\partial m_j^2(N)} \right)^2 \quad (42)$$

$$\eta_4 = \frac{E(N)/5}{R_4 + \varepsilon}, \text{ where } R_4 = \sum_{j=1}^{6} \left(\frac{\partial E}{\partial net_j^2(N)} \frac{\partial net_j^2(N)}{\partial \sigma_{L\_j}^2(N)} \right)^2 \quad (43)$$

$$\eta_5 = \frac{E(N)/5}{R_5 + \varepsilon}, \text{ where } R_5 = \sum_{j=1}^{6} \left(\frac{\partial E}{\partial net_j^2(N)} \frac{\partial net_j^2(N)}{\partial \sigma_{R\_j}^2(N)} \right)^2 \quad (44)$$

where ε is a positive constant. The detailed proof can be found in the Appendix.

V. Experimental Results

The three-phase grid-connected experimental PV system schematic diagram is illustrated in Fig. 4. The values of θ_e, P and Q are obtained by the power calculation and PLL block. When the dual mode control method determines the operation mode to be at mode I, the control input of the boost converter is the difference between V_{pv}^* and V_{pv} to achieve MPPT operation, and the input of the active power control of the three-phase inverter is the difference between V_{dc}^* and V_{dc} to keep the DC-link bus voltage at the desired value. At mode II, the control input of the boost converter is the difference between V_{dc}^* and V_{pv} to keep the DC-link bus voltage at the desired value, and the input of the active power control of the three-phase inverter is the difference between P^* and P to keep the power balance between the boost converter and the three-phase inverter. The grid fault control block determines the mode selection, P^*, and Q^* when V_{sag} is greater than 0.1. The first PI controller (PI1) is adopted for the control loop of V_{pv} to regulate the control output v_{con}. The control loops of V_{dc} and Q introduce the second and the third PI controllers (PI2, PI3) or the first and the second TSKPFNN-AMF controllers (TSKPFNN-AMF1, TSKPFNN-AMF2) to regulate the control output i_q^* and i_d^* respectively.

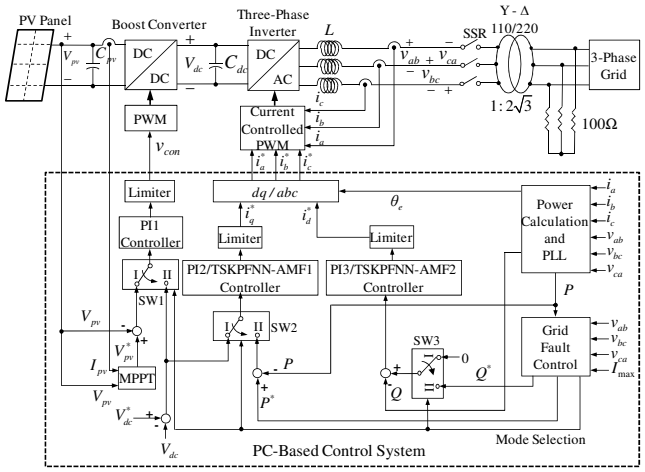

Fig. 4. Schematic diagram of experimental three-phase grid-connected PV system.

This article has been accepted for publication in a future issue of this journal, but has not been fully edited. Content may change prior to final publication. Citation information: DOI 10.1109/TIE.2015.2407851, IEEE Transactions on Industrial Electronics

The proposed TSKPFNN-AMF controller is realized using the "C" language under Windows operating system. The SIMULINK control package and TSKPFNN-AMF controller are integrated by using the S-function application programming interface of the SIMULINK. A 0.5ms sampling interval is used for the execution for all the control algorithms. Moreover, the processor of the PC is Intel Pentium G620 dual-core 2.6GHz, the RAM of the PC is 2048MB, and the hard disk volume is 300GB. The experimental control system is installed on a PC system for the convenience of parameters adjusting and programs debugging of the experimental control system. Thanks to the rapid progression in information technology, many PC-based DSP emulators are available and provide software development kit (SDK) to assist the developer to migrate the software codes from the PC into DSP-based system.

The transfer functions $G_{cn}(s)$ of these PI controllers can be generally expressed as $G_{cn}(s) = k_{pn} + k_{in}/s, n = 1, 2, 3$, where k_{pn} is the proportional gain and k_{in} is the integral gain. Moreover, the gains of these PI controllers $k_{p1}, k_{i1}, k_{p2}, k_{i2}, k_{p3}, k_{i3}$ are set to be 1, 1.5, 1.5, 2, 0.25, and 1.5. Furthermore, both the PI controller and the TSKPFNN-AMF controller are implemented in the experimentation for the comparison of the control performance. To measure the control performance of the mentioned controllers, the average tracking error T_{erravg} , the maximum tracking error T_{MAX} , the standard deviation of the tracking error T_σ [5] and the integral of squared error (ISE) of the tracking error T_{ISE} [24] for the command tracking are defined as follows:

$$T_{err}(N) = T^*(N) - T(N) \tag{45}$$

$$T_{MAX} = \max_N \left(\left| T_{err}(N) \right| \right) \tag{46}$$

$$T_\sigma = \sqrt{\frac{1}{m}\left(\sum_{N=1}^{m} \left(T_{err}(N) - T_{erravg} \right)^2 \right)}, T_{erravg} = \frac{1}{m}\left(\sum_{N=1}^{m} T_{err}(N) \right) \tag{47}$$

$$T_{ISE} = \int_0^\infty \{e(t)\}^2 dt \approx \Delta T \sum_{N=1}^{m} \left(T_{err}(N) \right)^2 \tag{48}$$

where $T^*(N)$ is the Nth value of the reference ($Q^*(N)$ or $V_{dc}^*(N)$) and $T(N)$ is the Nth value of the response ($Q(N)$ or $V_{dc}(N)$), and ΔT =0.5ms is the sampling interval of the system. The comparison of the control performance can be demonstrated by using the maximum tracking error and the ISE of the tracking error. The oscillation of the command tracking can be measured by the standard deviation of the tracking error.

The photograph of this experimental setup is shown in Fig. 5. Four emulated grid faults at PCC are selected in this study: *Case 1*) a two-phase to ground fault (sag type E) with 0.3pu voltage sag and assumed mode I operation, *Case 2*) a two-phase to ground fault with 0.7pu voltage sag and assumed mode II operation, *Case 3*) a two-phase to ground fault with 0.7pu voltage sag and assumed mode II operation at low irradiance condition, *Case 4*) a two-phase to ground unsymmetrical balance fault with 0.3pu and 0.5pu voltage sag and assumed mode II operation. In the experimentation, first, the grid line voltages are balanced and set at 1.0pu. At t=0.1s, the sag happens and the reactive power control is enabled. Moreover, in the experimentation, all the phase voltages are measured at the three-phase inverter side and the voltage sag phenomena (sag type F appears at inverter side) are different from the grid side due to the connected transformer.

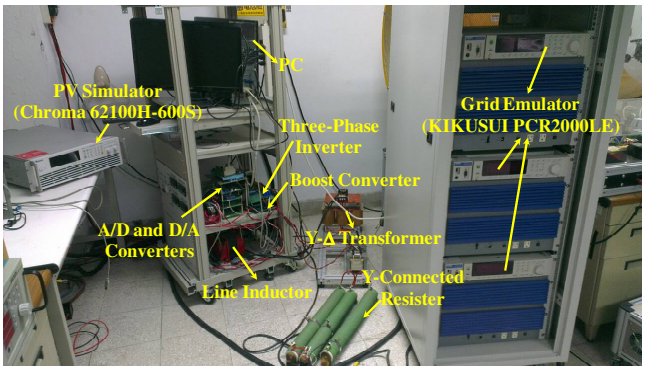

Fig. 5. Photograph of experimental setup.

A. Reactive Power Supporting at Mode I

Case 1):

In this case, the measured P, Q, Q^*, V_{dc}^*, V_{dc}, V_{pv}, I_{pv}, i_q^*, i_d^*, rms values of three-phase voltages and measured three-phase currents are shown in Fig. 6(a) for the PI controller and Fig. 6(b) for the TSKPFNN-AMF controller. In the beginning, P_{pv} is 612W and P is 524W due to the power losses in the boost converter and the three-phase inverter. Moreover, the amplitude of the inverter output currents is 4.1A. At t=0.1s, a two-phase to ground fault with 0.3pu voltage sag occurs on the grid side. Since the boost converter is operated in mode I, P remains unchanged and the amplitude of the three-phase inverter output currents increases to 6.4A. V_{pv} and I_{pv} remain unchanged due to normal operating of the MPPT control at mode I. Furthermore, Q rises to 456VAR; i_q^* changes from 4.1A to 4.9A; i_d^* rises to 2.9A; the three-phase voltages at the three-phase inverter side are 0.7pu, 0.87pu and 0.87pu, where 1.0pu = 63.5Vrms. From the experimental results, when the PI controllers are used, the settling time of Q and the overshoot of V_{dc} are about 0.45s and 4.9% respectively. On the other hand, the settling time of Q and the overshoot of V_{dc} are reduced to 0.3s and 1.45% respectively by using the TSKPFNN-AMF controllers. The results show that the settling time of Q is decreased by 33.3% and the overshoot of V_{dc} is decreased by 70.4% by using the TSKPFNN-AMF controllers. In addition, the injected three-phase currents are approximately balanced and without exceeding the maximum current limit. Additionally, as shown in Fig. 6, V_{pv} and I_{pv} are 150.9V and 4.05A respectively, and the maximum power point voltage of the PV panel V_{mpp} is 150.7V when the irradiance of the PV panel is set to 600W/m^2. Since V_{pv} is quite close to V_{mpp} , it can be inferred that the MPPT (mode I) control is operated correctly.

This article has been accepted for publication in a future issue of this journal, but has not been fully edited. Content may change prior to final publication. Citation information: DOI 10.1109/TIE.2015.2407851, IEEE Transactions on Industrial Electronics

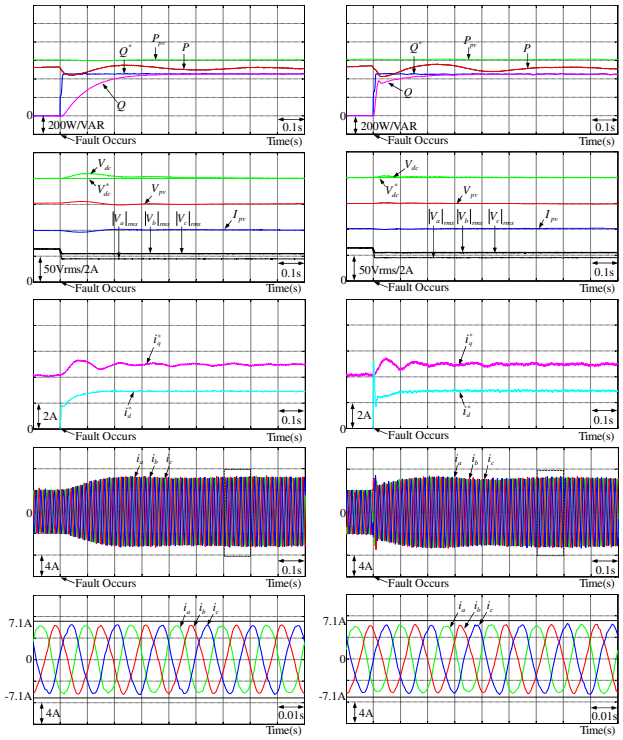

(a) (b)

Fig. 6. Experimental results of Case 1: (a) Using PI controllers. (b) Using TSKPFNN-AMF controllers.

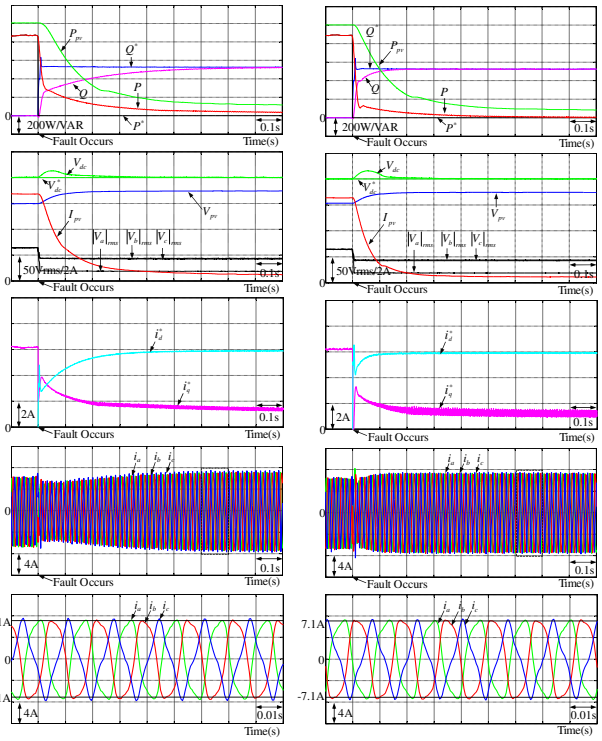

(a) (b)

Fig. 7. Experimental results of Case 2: (a) Using PI controllers. (b) Using TSKPFNN-AMF controllers.

B. Reactive Power Supporting at Mode II

Case 2):

In Case 2, the measured P, Q, P^*, Q^*, V_{dc}^*, V_{dc}, V_{pv}, I_{pv}, i_q^*, i_d^*, rms values of three-phase voltages and measured three-phase currents are shown in Fig. 7(a) for the PI controllers and Fig. 7(b) for the TSKPFNN-AMF controllers. In the beginning, P_{pv} is 1005W and P is 882W. At t=0.1s, a two-phase to ground fault with 0.7pu voltage sag occurs on the grid side. In order to limit the output three-phase currents to the maximum current limit, the operation mode of the boost converter is changed from mode I to mode II. Thus, P_{pv} drops to 102W and P drops to 21W. Moreover, Q rises to 527VAR; i_q^* drops from 6.2A to 1.3A; i_d^* rises to 5.9A; the three-phase voltages drop to 0.3pu, 0.67pu and 0.68pu. Furthermore, V_{pv} rises from 150.4V to 173.9V and I_{pv} drops from 6.6A to 0.52A due to the control operating at mode II for both the PI and TSKPFNN-AMF controllers. From the experimental results, when the PI controllers are used, the settling time of Q and the overshoot of V_{dc} are about 0.7s and 5.4% respectively. On the other hand, the settling time of Q is reduced to 0.16s by using the TSKPFNN-AMF controller and the overshoot of V_{dc} is 7% by using the PI1 controller. The results show that the settling time of Q is decreased by 77.1% by using the TSKPFNN-AMF controller. Therefore, based on the experimental results of Cases 1 and 2, the performance improvement of TSKPFNN-AMF controller is significant comparing with the PI controller. In addition, the maximum injection currents are still limited within the maximum current limit. However, the current distortion is worse than Case 1 due to severe unbalanced grid fault.

C. Reactive Power Supporting at Low Irradiance

Case 3):

In this case, the irradiance of PV panel is set to 100W/m^2. The boost converter and three-phase inverter still can operate normally. The measured P, Q, Q^*, V_{dc}^*, V_{dc}, V_{pv}, I_{pv}, i_q^*, i_d^*, rms values of three-phase voltages and measured three-phase currents are shown in Figs. 8(a) and 8(b) for the PI controllers and TSKPFNN-AMF controllers. In the beginning, P_{pv} is 106W and P is 63.8W. Moreover, the amplitude of the inverter output currents is 0.55A. At t=0.1s, a two-phase to ground fault with 0.7pu voltage sag occurs on the grid side. Therefore, in order to limit the output three-phase currents to the maximum current limit, the operation mode of the boost converter is changed from mode I to mode II. The amplitude of the output currents of the three-phase inverter increases to 7.5A. Furthermore, Q rises to 522VAR; i_q^* is still 1.3A; i_d^* rises to 5.9A; the three-phase voltages at the three-phase inverter side are 0.29pu, 0.67pu and 0.68pu. In addition, V_{pv} rises from 158V to 168V and I_{pv} drops from 0.67A to 0.46A due to the control operating at mode II for both the PI and TSKPFNN-AMF controllers. From the experimental results, when the PI controllers are used, the settling time of Q and the overshoot of V_{dc} are about 0.65s and 1.9% respectively. On the other hand, the settling time of Q is 0.2s by using the TSKPFNN-AMF controller and the overshoot of V_{dc} are about 1.4% by using the PI1 controller of the boost converter. Therefore, the grid-connected PV system can still supply the reactive power effectively during grid faults at low irradiance.

This article has been accepted for publication in a future issue of this journal, but has not been fully edited. Content may change prior to final publication. Citation information: DOI 10.1109/TIE.2015.2407851, IEEE Transactions on Industrial Electronics

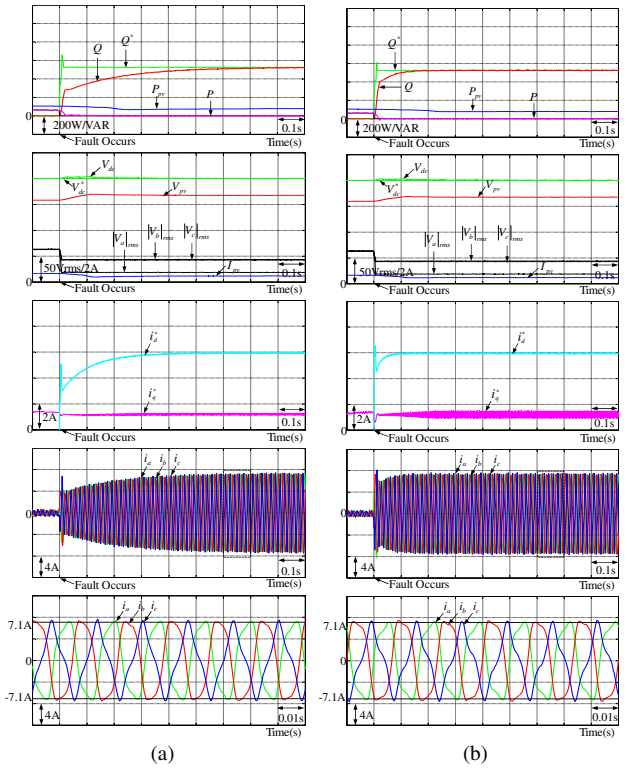

(a) (b)

Fig. 8. Experimental results of Case 3: (a) Using PI controllers. (b) Using TSKPFNN-AMF controllers.

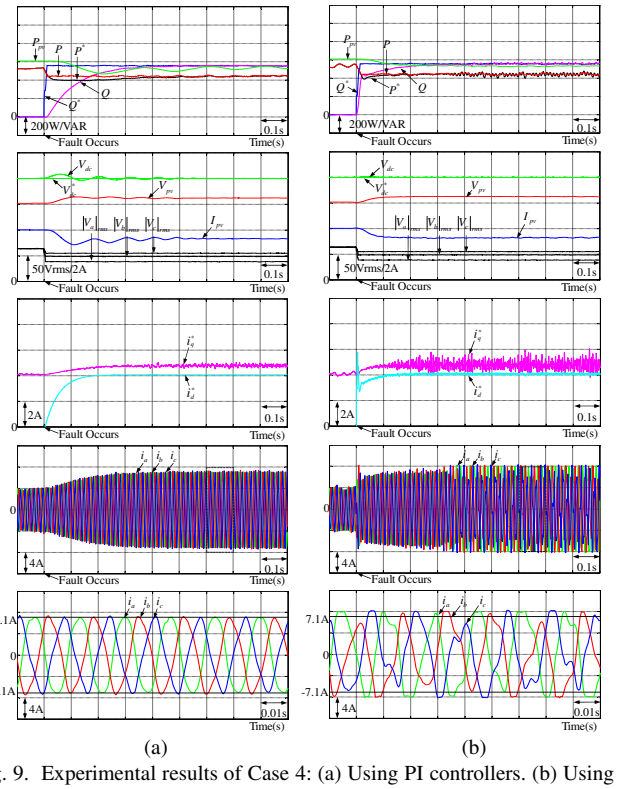

(a) (b)

Fig. 9. Experimental results of Case 4: (a) Using PI controllers. (b) Using TSKPFNN-AMF controllers.

D. Reactive Power Supporting at Unsymmetrical Unbalance Fault Condition

Case 4):

In this case, the measured P, Q, Q^*, V_{dc}^*, V_{dc}, V_{pv}, I_{pv}, i_q^*, i_d^*, rms values of three-phase voltages and measured three-phase currents are shown in Figs. 9(a) and 9(b) for the PI controllers and the TSKPFNN-AMF controllers. In the beginning, P_{pv} is 609W and P is 532W. At t=0.1s, two-phase to ground unsymmetrical balance fault with 0.3pu and 0.5pu voltage sag occurs on the grid side. Therefore, in order to limit the output three-phase currents to the maximum current limit, the operation mode of the boost converter is changed from mode I to mode II and the amplitude of the three-phase inverter output currents increases from 3.8A to 7.1A as shown in Fig. 9(a). Moreover, i_q^* changes from 4.1A to 4.9A; i_d^* rises to 4.1A; P_{pv} drops to 546W; P drops to 449W. Furthermore, the three-phase inverter injects 556VAR reactive power into grid and the three-phase voltages drop to 0.61pu, 0.77pu, and 0.86pu. In addition, V_{pv} rises from 152V to 162V and I_{pv} drops from 4.0A to 3.3A due to the control operating at mode II for both the PI and TSKPFNN-AMF controllers. From the experimental results, when the PI controllers are used, the settling time of Q and the overshoot of V_{dc} are about 0.45s and 4.1% respectively. On the other hand, the settling time of Q is 0.3s by using the TSKPFNN-AMF controller and the overshoot of V_{dc} is 0.6% by using the PI1 controller of the boost converter. Based on the experimental results of Cases 3 and 4, the performance improvement of TSKPFNN-AMF controller is also significant comparing with the PI controller.

TABLE II
THDS OF THREE-PHASE CURRENTS FOR CASE 1 TO CASE 4

Test Case	Controller	i_a(%)	i_b(%)	i_c(%)	Average (%)
Case 1	PI	8.73	8.72	7.16	8.20
	TSKPFNN-AMF	8.23	7.23	8.82	8.09
Case 2	PI	15.98	14.24	18.26	16.16
	TSKPFNN-AMF	16.90	16.55	21.45	18.30
Case 3	PI	17.59	16.62	21.87	18.69
	TSKPFNN-AMF	20.65	18.86	26.22	21.91
Case 4	PI	9.20	10.79	11.58	10.52
	TSKPFNN-AMF	19.99	25.74	34.20	26.64

The total harmonic distortions (THDs) of the three-phase currents for Case 1 to Case 4 are listed in Table II. In general, the TSKPFNN-AMF controllers result in higher THD. For instance, in Case 4, the THDs of i_a, i_b, and i_c are 9.2%, 10.79% and 11.58% when the PI controllers are used, and the THDs of i_a, i_b, and i_c are 19.99%, 25.74%, and 34.2% when the TSKPFNN-AMF controllers are used. Moreover, the computation, implementation and tuning of the proposed TSKPFNN-AMF controller are also more complex than the PI controller. Furthermore, since the TSKPFNN-AMF is a kind of neural networks, it also inherits the drawbacks of the neural networks. Disadvantages include greater computational burden, possibly converging to local minima, causing divergent results if the value of learning rate sets improperly, without exact rules for determining the number of layers and nodes, etc. In addition, from the experimental results shown in Figs. 6 to 9, there is no saturation phenomenon in all the control signals v_{con}, i_q^*, and i_d^* when the PI controllers are used. Thus, there is no anti-windup system on the PI controllers in this study.

From the experimental results of the previous cases, it can be stated that the proposed three-phase grid-connected

This article has been accepted for publication in a future issue of this journal, but has not been fully edited. Content may change prior to final publication. Citation information: DOI 10.1109/TIE.2015.2407851, IEEE Transactions on Industrial Electronics

PV system has clearly demonstrated the ability to deal with voltage sag while satisfying the LVRT regulation and to avoid exceeding current limit simultaneously. For the comparison of the control performance, a proportional-integral-differential (PID) controller, an FNN controller and a wavelet FNN (WFNN) controller [1] have been adopted in this study to replace the proposed TSKPFNN-AMF controller in the experimentation. The parameters of PID controllers are tuned by trial and error in this study to achieve the best control performance considering the stability requirement. Moreover, the FNN controller has a 4-layer structure with 2, 6, 9, and 1 neurons in its respective layer and the WFNN controller has a six-layer structure. The performance measurings of the PI, PID, FNN, WFNN and TSKPFNN-AMF controllers for the command tracking are shown in Fig. 10. by using (45) to (48). From the resulted performance measurings of PI, PID, FNN, WFNN and TSKPFNN-AMF controllers, the performances of TSKPFNN-AMF controllers are superior to the other controllers.

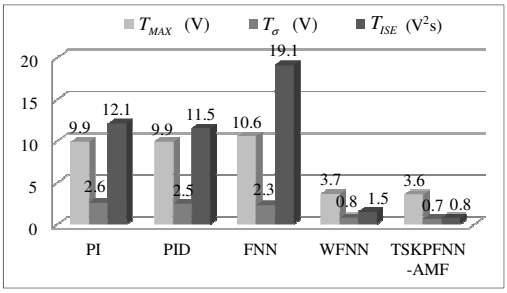

(a)

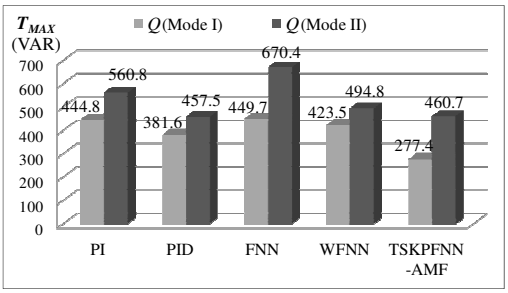

(b)

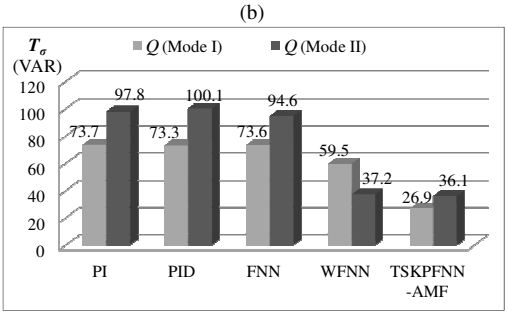

(c)

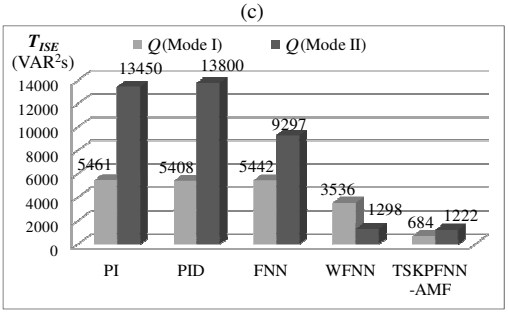

(d)

Fig. 10. Performance measurings: (a) Performance measuring of V_{dc} at mode I. (b) Performance measuring of Q using T_{MAX}. (c) Performance measuring of Q using T_σ. (d) Performance measuring of Q using T_{ISE}.

VI. CONCLUSIONS

This study has proposed an intelligent reactive and active power control using TSKPFNN-AMF controller for three-phase grid-connected PV system operating under voltage sags. First, the AC voltages and currents analyses of the grid-connected three-phase PV system during the grid faults were described. A dual mode operation control method is developed which effectively guarantees the active power balance between boost converter and three-phase inverter during grid faults. Moreover, the network structure, online learning algorithms and convergence analysis of the proposed TSKPFNN-AMF controller have discussed in detail. The analyses of experimental cases indicate that the proposed scheme is a good method to provide reactive current support for a grid-connected three-phase PV system during grid faults. Furthermore, the control performance of the intelligent control using TSKPFNN-AMF controller proved to be better than the control scheme using PI, PID, FNN and WFNN controllers via various performance measurings.

The contributions of this study are: 1) the development of the TSKPFNN-AMF controller and its online learning algorithms with convergence analysis; 2) the development of dual mode control for the grid-connected three-phase PV system; 3) the introduction of the TSKPFNN-AMF controller for the reactive and active power control to provide LVRT operation under various grid fault conditions.

APPENDIX

Considering the energy function in (22) as a discrete-type Lyapunov function, the change in the Lyapunov function can be written as

$$\Delta E(N) = E(N+1) - E(N) \tag{A1}$$

Then, the linearized model of the error equation can be represented via (24), (29), (33), (34), and (35) by

$$\begin{aligned} E(N+1) &= E(N) + \Delta E(N) \\ &\approx E(N) + \sum_{k=1}^{9}\left(\frac{\partial E(N)}{\partial w_k^6}\Delta w_k^6\right) \\ &\quad + \sum_{k=1}^{9}\sum_{i=1}^{2}\left(\frac{\partial E(N)}{\partial c_{ik}}\Delta c_{ik}\right) + \sum_{j=1}^{6}\left(\frac{\partial E(N)}{\partial m_j^2}\Delta m_j^2\right) \\ &\quad + \sum_{j=1}^{6}\left(\frac{\partial E(N)}{\partial \sigma_{L\_j}^2}\Delta\sigma_{L\_j}^2 + \frac{\partial E(N)}{\partial \sigma_{R\_j}^2}\Delta\sigma_{R\_j}^2\right) \\ &= \frac{E(N)}{5} - \eta_1\sum_{k=1}^{9}\left(\frac{\partial E}{\partial y_o^6(N)}\frac{\partial y_o^6(N)}{\partial w_k^6}\right)^2 \\ &\quad + \frac{E(N)}{5} - \eta_2\sum_{k=1}^{9}\sum_{i=1}^{2}\left(\frac{\partial E}{\partial T_k(N)}\frac{\partial T_k(N)}{\partial c_{ik}(N)}\right)^2 \\ &\quad + \frac{E(N)}{5} - \eta_3\sum_{j=1}^{6}\left(\frac{\partial E}{\partial net_j^2(N)}\frac{\partial net_j^2(N)}{\partial m_j^2(N)}\right)^2 \\ &\quad + \frac{E(N)}{5} - \eta_4\sum_{j=1}^{6}\left(\frac{\partial E}{\partial net_j^2(N)}\frac{\partial net_j^2(N)}{\partial \sigma_{L\_j}^2(N)}\right)^2 \\ &\quad + \frac{E(N)}{5} - \eta_5\sum_{j=1}^{6}\left(\frac{\partial E}{\partial net_j^2(N)}\frac{\partial net_j^2(N)}{\partial \sigma_{R\_j}^2(N)}\right)^2 \end{aligned} \tag{A2}$$

This article has been accepted for publication in a future issue of this journal, but has not been fully edited. Content may change prior to final publication. Citation information: DOI 10.1109/TIE.2015.2407851, IEEE Transactions on Industrial Electronics

where Δw_k^6 , Δc_{ik} , Δm_j^2 , $\Delta \sigma_{L\_j}^2$, $\Delta \sigma_{R\_j}^2$ represent the change of weight in the output layer, the change of weight in the TSK type fuzzy inference mechanism layer, and the change of the mean, left-sided, and right-sided standard deviation of the asymmetric Gaussian function in the membership layer. If the learning rates of the TSKPFNN-AMF controller are designed as (40) to (44), then (A2) can be rewritten as

$$E(N+1) \approx \varepsilon(\sum_{m=1}^{5}\eta_m) = \frac{E(N)\varepsilon/5}{R_1+\varepsilon} + \frac{E(N)\varepsilon/5}{R_2+\varepsilon} + \frac{E(N)\varepsilon/5}{R_3+\varepsilon} + \frac{E(N)\varepsilon/5}{R_4+\varepsilon} + \frac{E(N)\varepsilon/5}{R_5+\varepsilon} < E(N) \quad \text{(A3)}$$

According to (22) and (A3), if the learning rates of the TSKPFNN-AMF controller are designed as (40) to (44), the convergence of the proposed TSKPFNN-AMF controller can be guaranteed. Moreover, from (A1) and (A3), $\Delta E(N)$ is obtained as

$$\Delta E(N) \approx \varepsilon\left(\sum_{m=1}^{5}\eta_m\right) - E(N) = \frac{E(N)}{5}\left[\sum_{m=1}^{5}\left(\frac{\varepsilon}{R_m+\varepsilon}-1\right)\right] = -\frac{E(N)}{5}\left[\sum_{m=1}^{5}\left(\frac{R_m}{R_m+\varepsilon}\right)\right] < 0 \quad \text{(A4)}$$

Therefore, the proof of the convergence of TSKPFNN-AMF controller is completed.

REFERENCES

[1] C. H. Lu, "Wavelet fuzzy neural networks for identification and predictive control of dynamic systems," *IEEE Trans. Ind. Electron.*, vol. 58, no. 7, pp. 3046-3058, Jul. 2011.

[2] W. M. Lin and C. M. Hong, "Neural-network-based MPPT control of a stand-alone hybrid power generation system," *IEEE Trans. Power Electron*., vol. 26, no. 12, pp. 3571-3581, Dec. 2011.

[3] Y. Y. Lin, J. Y. Chang, and C. T. Lin, "A TSK-type-based self-evolving compensatory interval type-2 fuzzy neural network (TSCIT2FNN) and its applications," *IEEE Trans. Ind. Electron*., vol. 61, no. 1, pp. 447-459, Jan. 2014.

[4] C. M. Lin and H. Y. Li, "TSK fuzzy CMAC-based robust adaptive backstepping control for uncertain nonlinear systems," *IEEE Trans. Fuzzy Syst*., vol. 20, no. 6, pp. 1147-1154, Dec. 2012.

[5] F. J. Lin, Y. C. Hung, and M. T. Tsai, "Fault-tolerant control for six-phase PMSM drive system via intelligent complementary sliding-mode control using TSKFNN-AMF," *IEEE Trans. Ind. Electron*., vol. 60, no. 12, pp. 5747-5762, Dec. 2013.

[6] Z. Liu and H. X. Li, "A probabilistic fuzzy logic system for modeling and control," *IEEE Trans. Fuzzy Syst.*, vol. 13, no. 6, pp. 848-859, Dec. 2005.

[7] F. J. Lin, M. S. Huang, P. Y. Yeh, H. C. Tsai, and C. H. Kuan, "DSP-based probabilistic fuzzy neural network control for Li-ion battery charger," *IEEE Trans. Power Electron*., vol. 27, no. 8, pp. 3782-3794, Aug. 2012.

[8] Y. Bae, T. K. Vu, and R. Y. Kim, "Implemental control strategy for grid stabilization of grid-connected PV system based on German grid code in symmetrical low-to-medium voltage network," *IEEE Trans. Energy Convers.*, vol. 28, no. 3, pp.619-631, Sep. 2013.

[9] M. H. J. Bollen, "Characterisation of voltage sags experienced by three-phase adjustable-speed drives," *IEEE Trans. Power Del.*, vol. 12, no. 4, pp. 1666-1671, Oct. 1997.

[10] P. Thakur and A. K. Singh, "Unbalance voltage sag fault-type characterization algorithm for recorded waveform," *IEEE Trans. Power Del*., vol. 28, no. 2, pp. 1007-1014, Apr. 2013.

[11] *Grid code-high and extra high voltage*, E.ON Netz GmbH. Bayreuth, Company, Apr. 2006, pp. 14-19.

[12] P. Rodriguez, A. V. Timbus, R. Teodorescu, M. Liserre, and F. Blaabjerg, "Flexible active power control of distributed power generation systems during grid faults," *IEEE Trans. Ind. Electron.*, vol. 54, no. 5, pp. 2583-2592, Oct. 2007.

[13] S. Alepuz, S. Busquets-Monge, J. Bordonau, J. A. Martinez-Velasco, C. A. Silva, J. Pontt, and J. Rodriguez, "Control strategies based on symmetrical components for grid-connected converters under voltage dips," *IEEE Trans. Ind. Electron.*, vol. 56, no. 6, pp. 2162-2173, Jun. 2009.

[14] J. Miret, M. Castilla, A. Camacho, L. García de Vicuña, and J. Matas, "Control scheme for photovoltaic three-phase inverters to minimize peak currents during unbalanced grid-voltage sags," *IEEE Trans. Power Electron*., vol. 27, no. 10, pp. 4262-4271, Oct. 2012.

[15] A. Camacho, M. Castilla, J. Miret, J. C. Vasquez, and E. Alarcon-Gallo, "Flexible voltage support control of three-phase distributed generation inverters under grid fault," *IEEE Trans. Ind. Electron.*, vol. 60, no. 4, pp. 1429-1441, Apr. 2013.

[16] J. Miret, A. Camacho, M. Castilla, L. García de Vicuña, and J. Matas, "Control scheme with voltage support capability for distributed generation inverters under voltage sags," *IEEE Trans. Power Electron*., vol. 28, no. 11, pp. 5252-5262, Nov. 2013.

[17] X. Guo, X. Zhang, B. Wang, W. Wu, and J. M. Guerrero, "Asymmetrical grid fault ride through strategy of three-phase grid-connected inverter considering network impedance impact in low-voltage grid," *IEEE Trans. Power Electron.*, vol. 29, no. 3, pp. 1064-1068, Mar. 2014.

[18] S. F. Chou, C. T. Lee, H. C. Ko, and P. T. Cheng, "A low-voltage ride-through method with transformer flux compensation capability of renewable power grid-side converters," *IEEE Trans. Power Electron.*, vol. 29, no. 4, pp. 1710-1719, Apr. 2014.

[19] M. A. Gomes de Brito, L. G. Jr., L. P. Sampaio, G. de Azevedo e Melo, and C. A. Canesin, "Evaluation of the main MPPT techniques for photovoltaic applications," *IEEE Trans. Ind. Electron.*, vol. 60, no. 3, pp. 1156-1166, Mar. 2013.

[20] F. Z. Peng and J. S. Lai, "Generalized instantaneous reactive power theory for three-phase power systems," *IEEE Trans. Instrum. Meas.*, vol. 45, no. 1, pp. 293-297, Feb. 1996.

[21] R. Teodorescu, M. Liserre, and P. Rodriguez, *Grid converters for photovoltaic and wind power systems*. John Wiley & Sons. Ltd. 2011, pp. 219-221.

[22] N. Sozhamadevi, R. S. Lourdu Delcause, and S. Sathiyamoorthy, "Design and implementation of probabilistic fuzzy logic control system," *IEEE 2012 Inter. Conf. Emerging Trends in Science, Engineering and Technology*, pp. 523-531, 2012.

[23] D. F. Specht, "Probabilistic neural network," *Neural Networks*, vol. 3, no. 1, pp. 109-118, 1990.

[24] K. V. Ling, W. K. Ho, Y. Feng, and B. F. Wu, "Integral-square error performance of multiplexed model predictive control," *IEEE Trans. Ind. Informat.*, vol. 7, no. 2, pp. 196-203, May 2011.

Faa-Jeng Lin (M'93–SM'99) received his Ph.D. degree in electrical engineering from National Tsing Hua University, Taiwan, in 1993. Currently, he is Chair Professor, Department of Electrical Engineering, National Central University, Taiwan. He was the Chair of the Power Engineering Division at the National Science Council in Taiwan and the Chair of the IEEE IE/PELS Taipei Chapter from 2007 to 2009. He was also of the chair of IEEE CIS Taipei Chapter, 2012 to 2014. He received the Outstanding Research Award from the National Science Council, Taiwan, in 2004, 2010 and 2013; the Outstanding Professor of Electrical Engineering Award in 2005 from the Chinese Electrical Engineering Association, Taiwan. Moreover, he is a Fellow of the Institution of Engineering and Technology (IET). His research interests include fuzzy and neural network control theories, nonlinear control theories, AC and ultrasonic motor drives, DSP-based computer control systems, power electronics, microgrid and smart grid.

Kuang-Chin Lu (M'13) received the B.S. and M.S. degrees from National Cheng Kung University, Tainan, Taiwan, both in electrical engineering, in 1986 and 1988, respectively. He is currently working toward the Ph.D. degree in electrical engineering, National Central University, Chungli, Taiwan.

From 1999 to now, he is a Senior Researcher with the Telecommunication Laboratories, Chunghwa Telecom Co., Ltd., Taoyuan, Taiwan. Moreover, he received the Outstanding Engineer Award in 2014 from the Chinese Institute of Engineers, Taiwan. His research interests include power electronics, energy saving technologies, grid-connected PV system, power system fault analysis and intelligence control theories.

This article has been accepted for publication in a future issue of this journal, but has not been fully edited. Content may change prior to final publication. Citation information: DOI 10.1109/TIE.2015.2407851, IEEE Transactions on Industrial Electronics

Ting-Han Ke was born in Taichung, Taiwan, in 1988. He received the B.S. degree in electrical engineering from National Chiao Tung University, Hsinchu, Taiwan, and M.S. degree in electrical engineering from the National Central University, Chungli, Taiwan in 2010 and 2013 respectively. His research interests include low voltage ride through, reactive power control and intelligence control theories.

Bo-Hui Yang received the B.S. degree in electrical engineering from National United University, Miaoli, Taiwan, in 2014. He is currently working toward the M.S. degree in electrical engineering, National Central University, Chungli, Taiwan. His research interests include PV system maximum power point tracking, intelligent control theories and technical analysis of low voltage ride through.

Yung-Ruei Chang (M'01) received his Ph.D. degree in electrical engineering from National Taiwan University in 2004. He is now the Deputy Director of Nuclear Instrumentation Division of the Institute of Nuclear Energy Research (INER), Atomic Energy Council, Taiwan, where he has been working since 1994. Since 2005, he has been responsible for power conditioning systems of the renewable energy project and leaded the distributed generation research group of INER. In 2007, he was a visiting scholar at Future Energy Electronics Center of Virginia Polytechnic and State University, USA, where he joined to develop a high-efficiency DC-DC converter for solid oxide fuel cell. Now he is in charge of microgrid project of INER. His research interests include microgrid technology, power electronic system, dependable computing, system reliability analysis and fault-tolerant system. He is a member of the IEEE.